PHY392S
Physics of Climate

Lectures 13 - 14

Supplementary slides

Positive and Negative feedbacks in the Climate System

Positive Feedback

Water vapour feedback

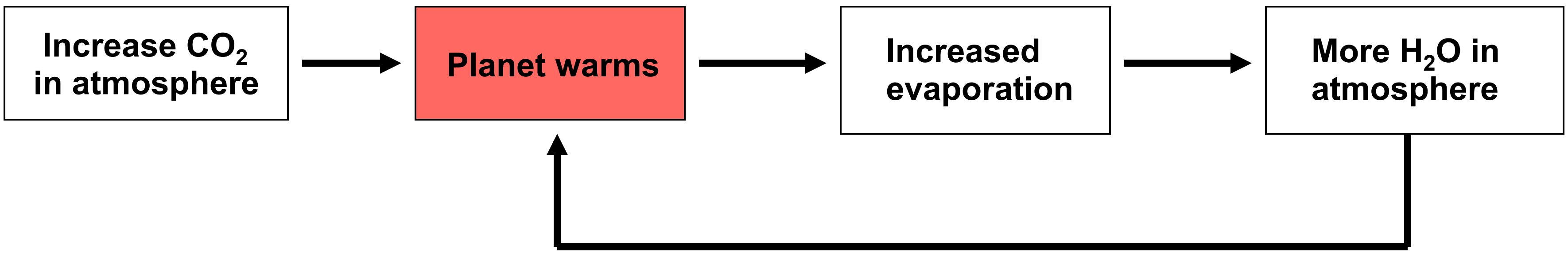

Albedo feedback

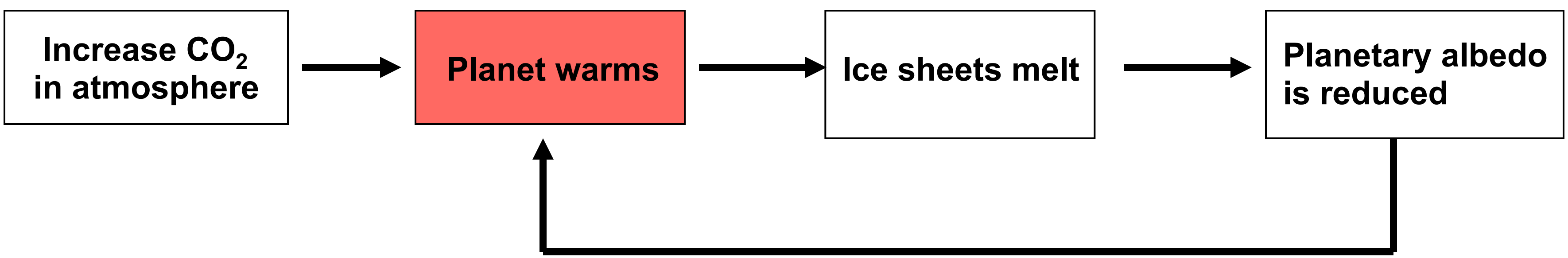

Water Vapour Feedback

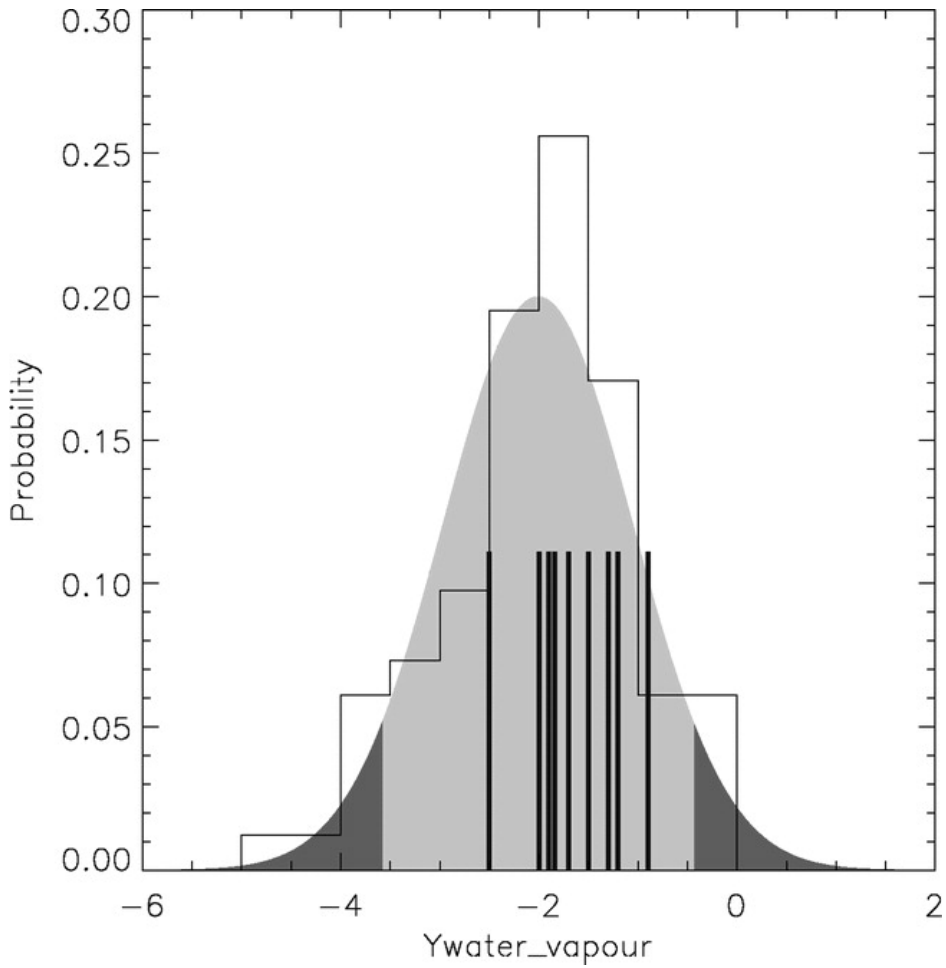

- The histogram is based on 82 model estimates, with a fitted curve indicated by the shading.
- Observed estimates of the water vapor feedback parameter are indicated by the vertical lines, and lie in the range 0.9–2.5 W m^{-2} K^{-1} (Boney et al., 2006)

[Bony et al., 2006]

The distribution of the uncertainty in the feedback is fairly Gaussian, unlike the distribution of the climate sensitivity

Climate Sensitivity Distribution

Fig. 1. Demonstration of the relationships linking $h_T(\Delta T)$ to $h_f(f)$. ΔT_0 is the sensitivity in the absence of feedbacks. If the mean estimate of the total feedbacks is substantially positive, any distribution in $h_f(f)$ will lead to a highly skewed distribution in ΔT. For the purposes of illustration, a normal distribution in $h_f(f)$ is shown with a mean of 0.65 and a SD of 0.13, typical to that obtained from feedback studies of GCMs (*17*, *18*). The dot-dashed lines represent 95% confidence intervals on the distributions. Note that values of $f \geq 1$ imply an unphysical, catastrophic runaway feedback.

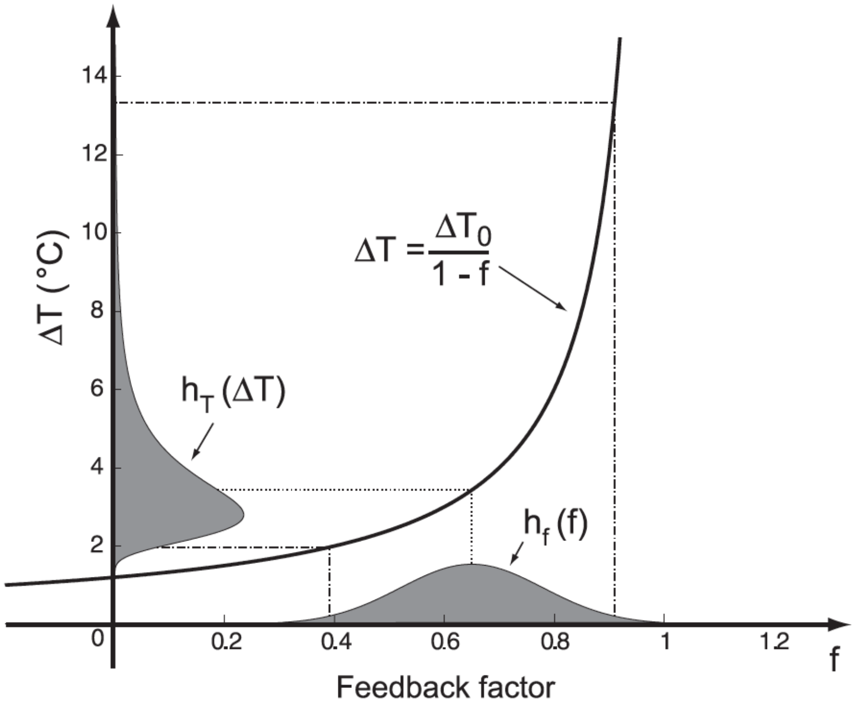

[Roe and Baker, 2007]

$$h_f(f) = \left(\frac{1}{\sigma_f\sqrt{2\pi}}\right)exp\left[-\frac{1}{2}\left(\frac{(f-\bar{f})}{\sigma_f}\right)^2\right].$$

$$h_T(\Delta T) = \left(\frac{1}{\sigma_f\sqrt{2\pi}}\right)\frac{\Delta T_0}{\Delta T^2}\ exp\left[-\frac{1}{2}\left(\frac{(1-\bar{f}-\frac{\Delta T_0}{\Delta T})}{\sigma_f}\right)^2\right]$$

Climate Sensitivity Distribution

Fig. 3. Climate sensitivity distributions: (**A**) from (*18*), which calculated ($\bar{f}$, σ_f) of (0.62, 0.13) from a suite of GCM simulations; (**B**) from (*17*), which found ($\bar{f}$, σ_f) of (0.7, 0.14) from a different suite of models; and (**C**) from the ~5700-member multi-ensemble climateprediction.net (*9*, *10*) for different choices of cloud processes. [Data were provided courtesy of B. M. Sanderson] (**D**) Fit of Eq. 3 to the result of (*10*), which was found by estimating the mode of the probability density and its accompanying ΔT and solving for ($\bar{f}$, σ_f) from Eqs. 2 and 3, which yielded values of (0.67, 0.12).

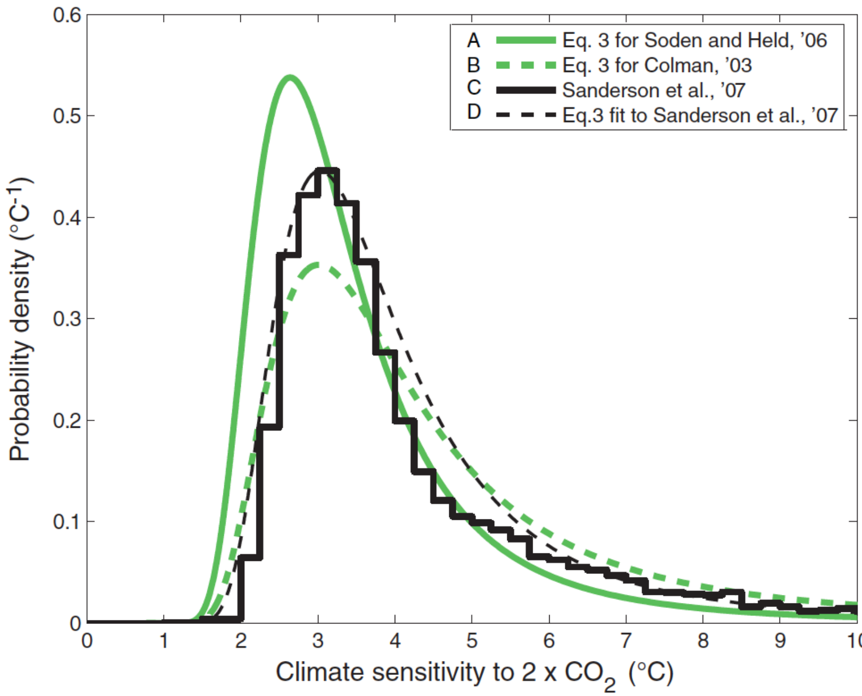

[Roe and Baker, 2007]

Distribution based on equation from Roe and Baker

Climate Feedback Parameters

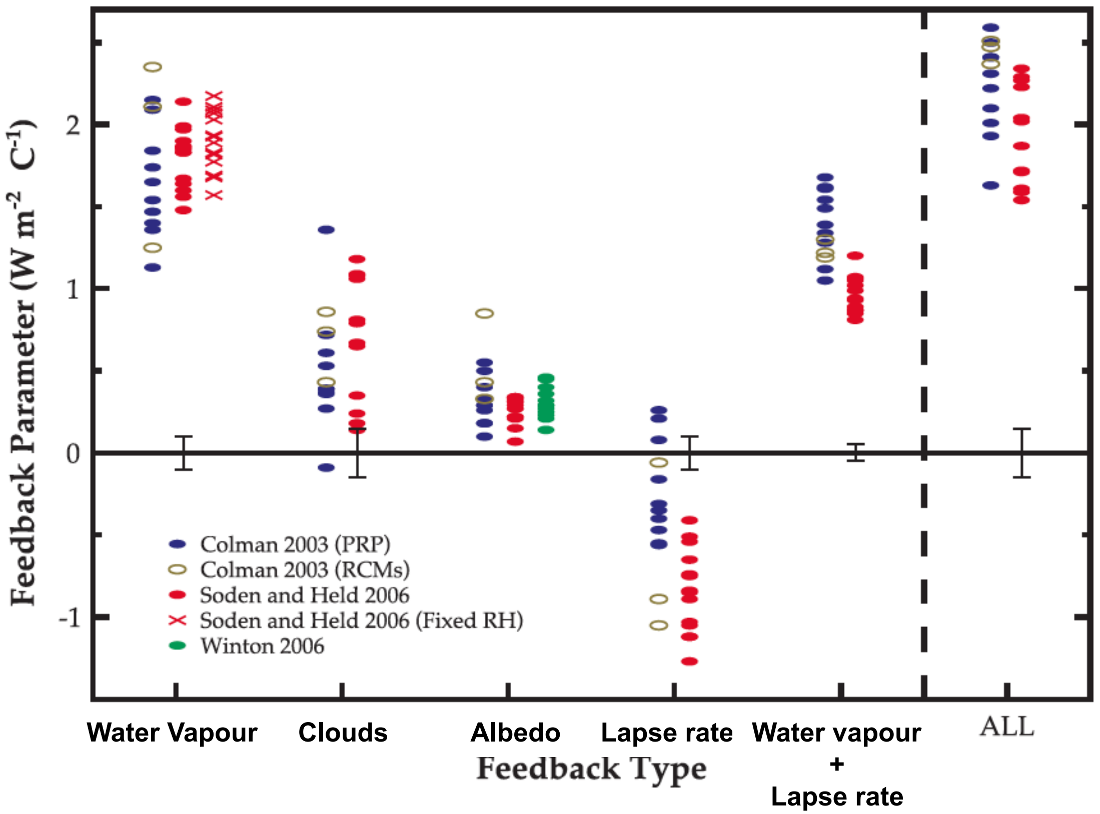

Figure 8.14. *Comparison of GCM climate feedback parameters for water vapour (WV), cloud (C), surface albedo (A), lapse rate (LR) and the combined water vapour plus lapse rate (WV + LR) in units of W m^{-2} °C^{-1}. 'ALL' represents the sum of all feedbacks. Results are taken from Colman (2003a; blue, black), Soden and Held (2006; red) and Winton (2006a; green). Closed blue and open black symbols from Colman (2003a) represent calculations determined using the partial radiative perturbation (PRP) and the radiative-convective method (RCM) approaches respectively. Crosses represent the water vapour feedback computed for each model from Soden and Held (2006) assuming no change in relative humidity. Vertical bars depict the estimated uncertainty in the calculation of the feedbacks from Soden and Held (2006).*

[IPCC, 2007]

Climate Feedback Parameters: Lapse rate and water vapor

TABLE 2. Tabulated values of the feedback parameters from the CMIP-II model archive. The data required for computing the surface albedo feedback were not available from the archive.

	Planck	Lapse rate	Water vapor
CCCM	−3.18	−0.51	1.61
CSIR	−3.24	−0.42	1.68
CSM	−3.21	−0.76	1.62
GFDL	−3.25	−0.62	1.73
ECHO	−3.28	−1.48	2.23
ECHAM	−3.23	−1.36	2.20
HAD2	−3.25	−1.15	1.83
HAD3	−3.21	−0.75	1.51
MRI	−3.24	−1.00	2.09
PCM	−3.16	−0.66	1.62

[Soden and Held, 2006]

Models with strong, negative lapse rate feedback also typically large, positive water vapour feedback

Observational determination of albedo decrease caused by vanishing Arctic sea ice

Kristina Pistone, Ian Eisenman[1], and V. Ramanathan

Scripps Institution of Oceanography, University of California, San Diego, La Jolla, CA 92093-0221

Edited by Gerald R. North, Texas A&M University, College Station, TX 77843, and accepted by the Editorial Board January 6, 2014 (received for review September 30, 2013)

The decline of Arctic sea ice has been documented in over 30 y of satellite passive microwave observations. The resulting darkening of the Arctic and its amplification of global warming was hypothesized almost 50 y ago but has yet to be verified with direct observations. This study uses satellite radiation budget measurements along with satellite microwave sea ice data to document the Arctic-wide decrease in planetary albedo and its amplifying effect on the warming. The analysis reveals a striking relationship between planetary albedo and sea ice cover, quantities inferred from two independent satellite instruments. We find that the Arctic planetary albedo has decreased from 0.52 to 0.48 between 1979 and 2011, corresponding to an additional 6.4 $\pm$ 0.9 W/m^2 of solar energy input into the Arctic Ocean region since 1979. Averaged over the globe, this albedo decrease corresponds to a forcing that is 25% as large as that due to the change in CO_2 during this period, considerably larger than expectations from models and other less direct recent estimates. Changes in cloudiness appear to play a negligible role in observed Arctic darkening, thus reducing the possibility of Arctic cloud albedo feedbacks mitigating future Arctic warming.

we assess the magnitude of planetary darkening due to Arctic sea ice retreat, providing a direct observational estimate of this effect. We then compare our estimate with simulation results from a state-of-the-art ocean–atmosphere global climate model (GCM) to determine the ability of current models to simulate these complex processes.

Comparing spatial patterns of the CERES clear-sky albedo with SSM/I sea ice concentration patterns, we find a striking resemblance (Fig. 1), revealing that the spatial structure of planetary albedo is dominated by sea ice cover both in terms of the time average (Fig. 1 *A* and *B*) and the changes over time (Fig. 1 *C* and *D*). Fig. 1 focuses on the month of September, when the year-to-year sea ice decline has been most pronounced, although there is also agreement between sea ice cover and planetary albedo during every other sunlit month of the year (Fig. S1). There is also a smaller effect associated with diminishing albedo in central Arctic regions which have nearly 100% sea ice cover throughout the record (Fig. 1*D* and Fig. S1), as would be expected from a warming ice pack experiencing more surface melt (16).

EARTH, ATMOSPHERIC, AND PLANETARY SCIENCES

www.pnas.org/cgi/doi/10.1073/pnas.1318201111

CERES: Clouds and Earth's Radiant Energy System
SSM/I: Special Sensor Microwave/Image (on the Defense Meteorological Satellite Program satellites

Pistone et al. (2014), Observational determination of albedo decrease caused by vanishing Arctic sea ice.

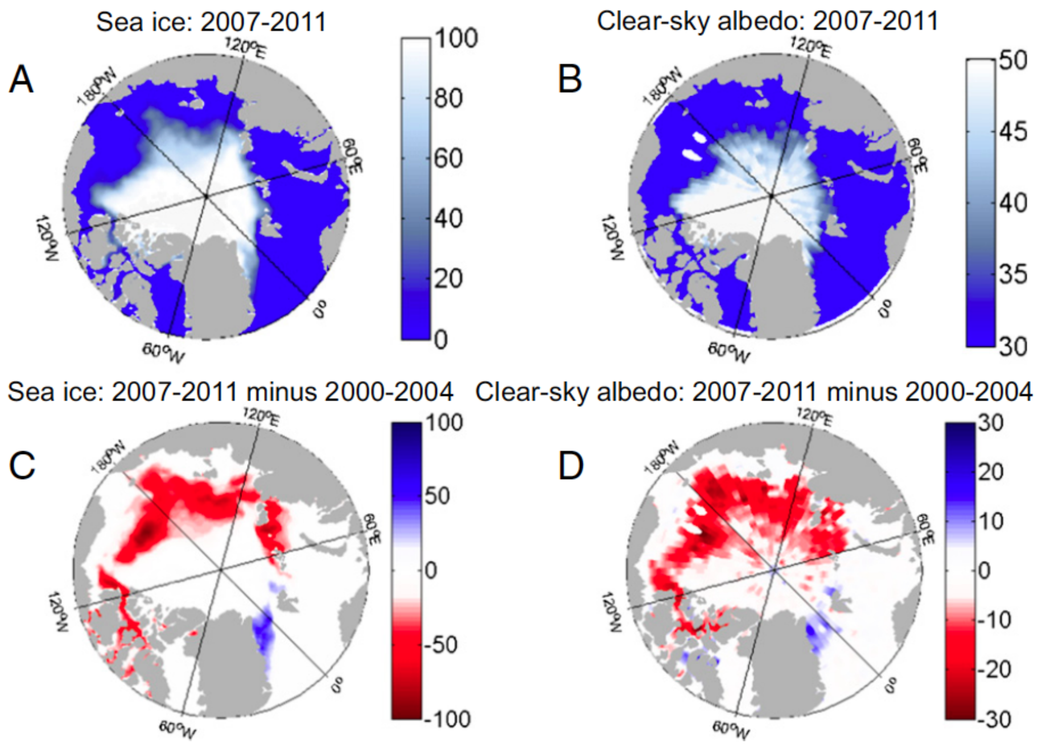

Fig. 1. (*A*) Sea ice concentration and (*B*) CERES clear-sky albedo averaged over each September during the last 5 y of the CERES record (2007–2011) and the change in (*C*) sea ice and (*D*) clear-sky albedo between the mean of the last five Septembers (2007–2011) and the mean of the first five Septembers (2000–2004) of the CERES record. Results for other months are included in Fig. S1.

Pistone et al. (2014), Observational determination of albedo decrease caused by vanishing Arctic sea ice.

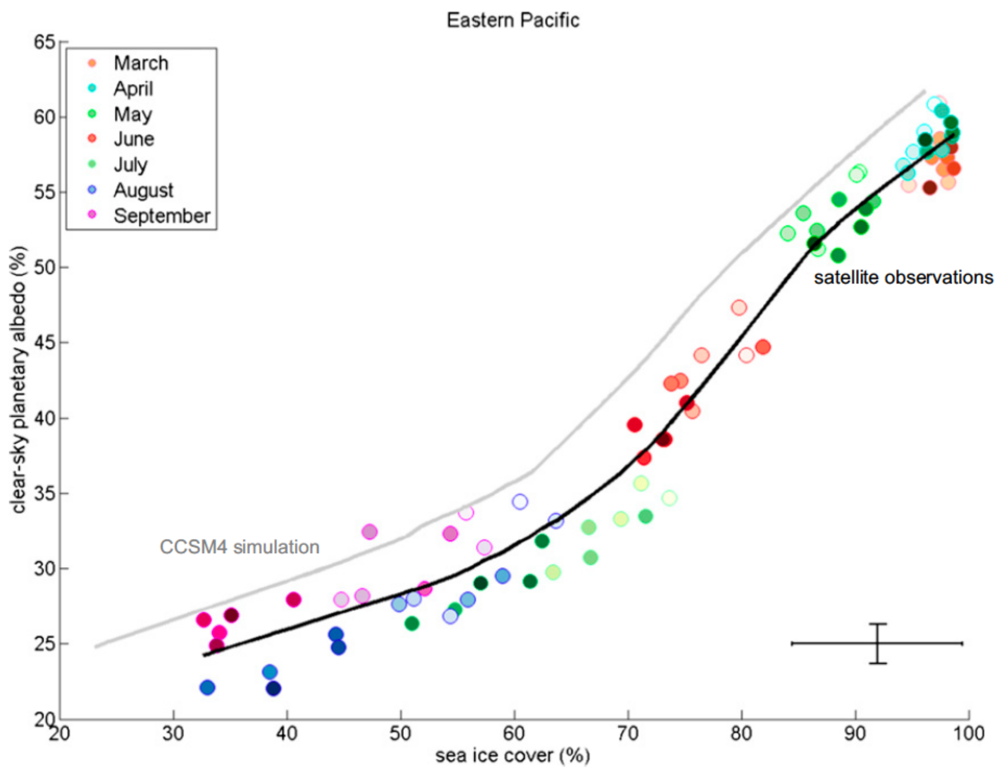

Fig. 2. Monthly mean CERES clear-sky planetary albedo versus SSM/I sea ice cover for the months March through September during 2000–2011 in the Eastern Pacific (EP) region. Different colors indicate different months, and lighter shading indicates earlier years. The thick black line indicates smoothing with a lowpass moving average filter with a span of 41 points. NCAR CCSM4 model output for the same region is also included (gray line), using simulation years 1985–2005 smoothed with a lowpass moving average filter with a span of 82 points (widened to account for the longer time series). The error bar in the bottom right corner indicates the instrumental uncertainty of both datasets (*Supporting Information*).

Pistone et al. (2014), Observational determination of albedo decrease caused by vanishing Arctic sea ice.

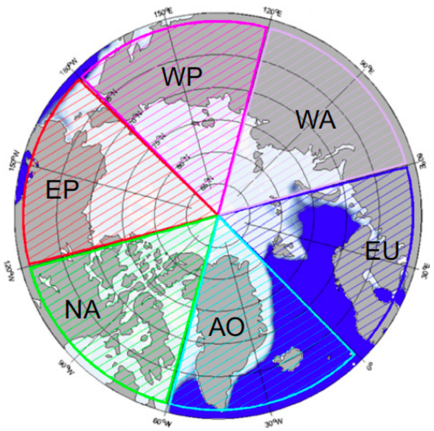

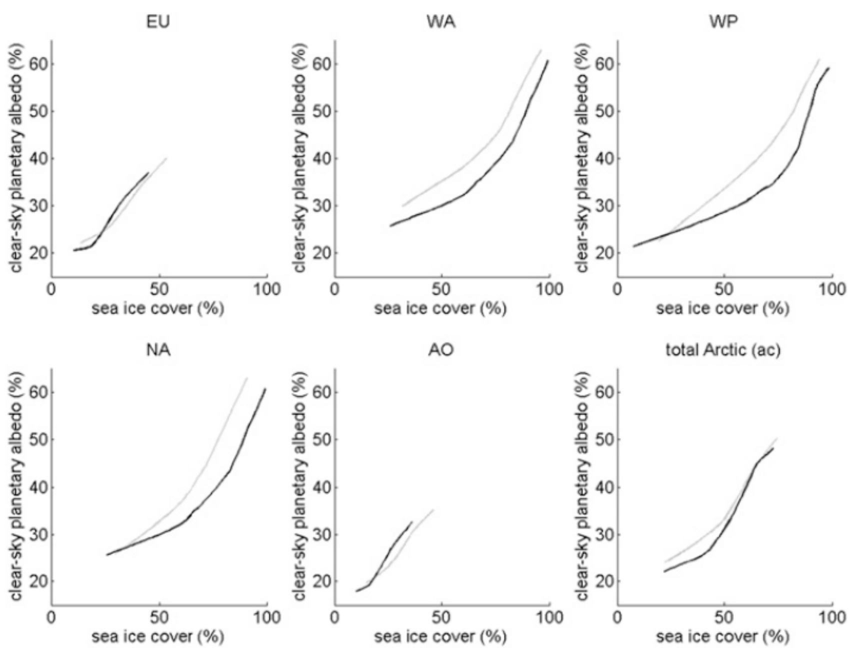

Fig. S4. As in Fig. 2, but for the other regions defined in Fig. S2 as well as for the total Arctic. Note that CCSM4 gives results fairly similar to CERES, although the change in slope occurring around June is less pronounced in the model output, and the model gives a higher summer minimum albedo.

Pistone et al. (2014), Observational determination of albedo decrease caused by vanishing Arctic sea ice.

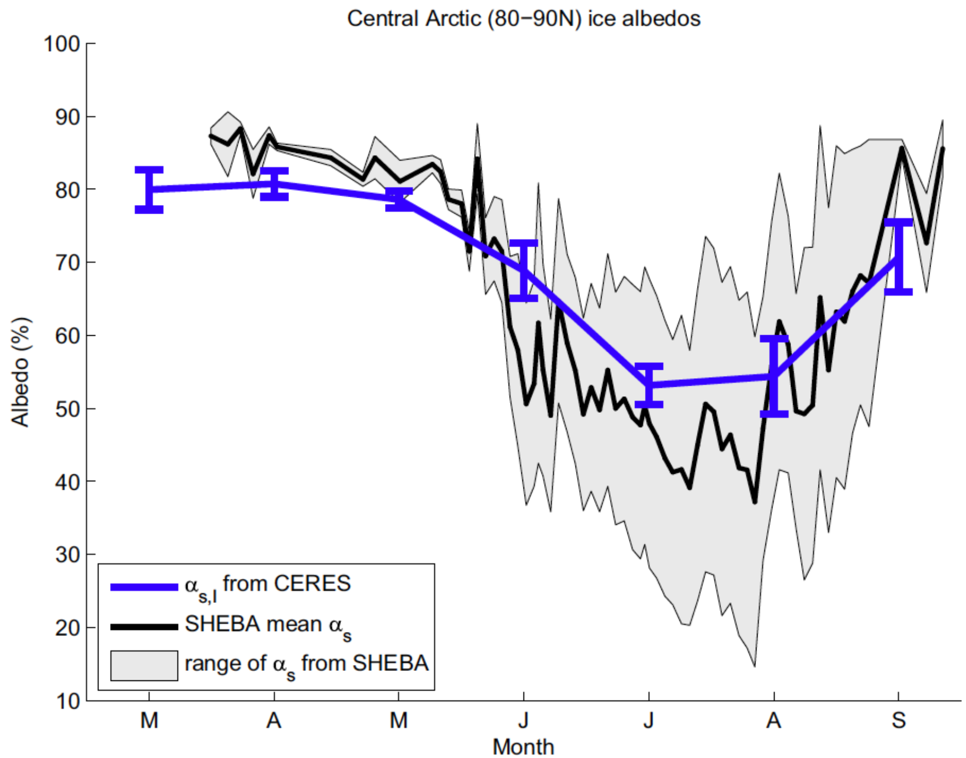

Fig. 3. The mean seasonal cycle in sea ice surface albedo during 2000–2011 derived from the CERES data in the region 80–90°N (blue line) and from in situ surface albedo measurements from the Surface Heat Budget of the Arctic (SHEBA) project (18) of 1997–1998 (black line). Blue error bars indicate one SD of CERES 2000–2011 year-to-year variability, and gray shading indicates one SD of SHEBA spatial variability along a 200-m survey line.

Pistone et al. (2014), Observational determination of albedo decrease caused by vanishing Arctic sea ice.

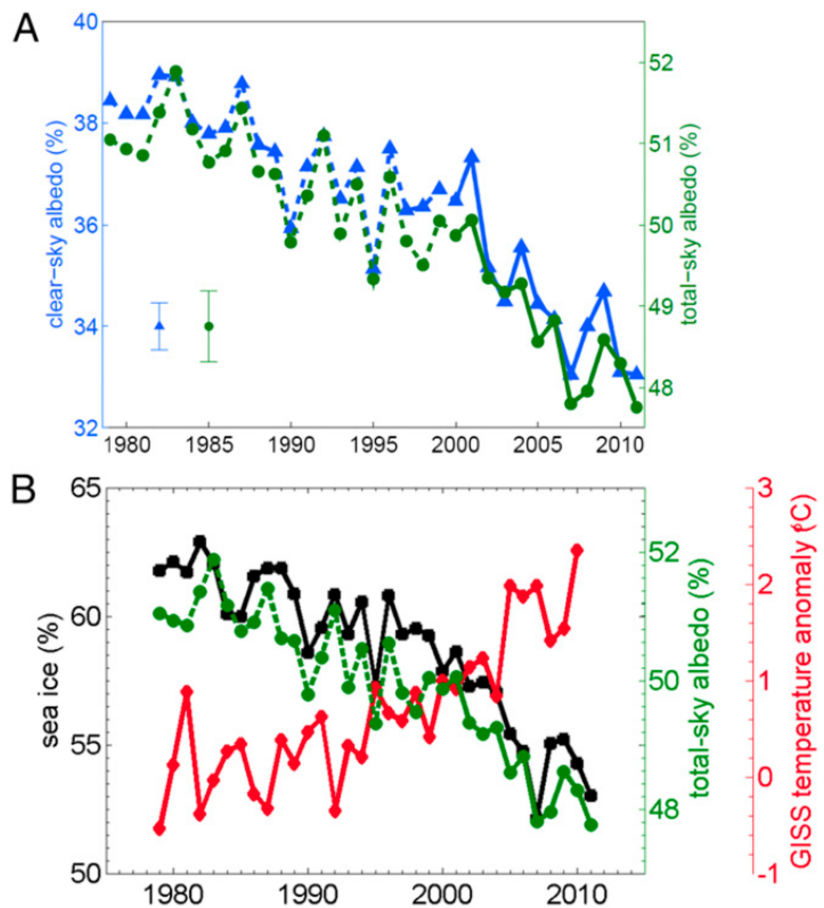

Fig. 4. (*A*) Observed annual-mean clear-sky and all-sky planetary albedo for the entire Arctic region. Solid lines are direct CERES observations, and dashed lines are estimates derived from sea ice observations. The error bars in the *Bottom Left* corner indicate the uncertainty in the pre-CERES clear-sky and all-sky albedo values (*Supporting Information*). (*B*) All-sky albedo as in *A* compared with annual-mean observed sea ice area (as a fraction of the ocean in the Arctic region) and surface air temperature averaged over the ocean in the Arctic region.